Astronomy & Astrophysics

Special feature

OSIRIS observations of meter-sized exposures of H₂O ice at the surface of 67P/Churyumov-Gerasimenko and interpretation using laboratory experiments

A. Pommerol[1], N. Thomas[1], M. R. El-Maarry[1], M. Pajola[2], O. Groussin[3], A.-T. Auger[3], N. Oklay[4], S. Fornasier[5],
C. Feller[5], B. Davidsson[6], A. Gracia-Berná[1], B. Jost[1], R. Marschall[1], O. Poch[1], M. A. Barucci[5], J.-L. Bertaux[7],
F. La Forgia[8], H. U. Keller[9,10], E. Kührt[9], S. C. Lowry[11], S. Mottola[9], G. Naletto[2,12,13], H. Sierks[4], C. Barbieri[8],
P. L. Lamy[3], R. Rodrigo[14,15], D. Koschny[16], H. Rickman[6,17], J. Agarwal[4], M. F. A'Hearn[18], I. Bertini[2], S. Boudreault[4],
G. Cremonese[19], V. Da Deppo[13], M. De Cecco[20], S. Debei[21], C. Güttler[4], M. Fulle[22], P. J. Gutierrez[22], S. F. Hviid[9],
W.-H. Ip[24], L. Jorda[3], J. Knollenberg[9], G. Kovacs[4], J.-R. Kramm[4], E. Küppers[25], L. Lara[23], M. Lazzarin[8],
J. L. Lopez Moreno[23], F. Marzari[8], H. Michalik[26], F. Preusker[9], F. Scholten[9], C. Tubiana[4], and J.-B. Vincent[4]

(Affiliations can be found after the references)

ABSTRACT

Since OSIRIS started acquiring high-resolution observations of the surface of the nucleus of comet 67P/Churyumov-Gerasimenko, over one hundred meter-sized bright spots have been identified in numerous types of geomorphologic regions, but mostly located in areas receiving low insolation. The bright spots are either clustered, in debris fields close to decameter-high cliffs, or isolated without structural relation to the surrounding terrain. They can be up to ten times brighter than the average surface of the comet at visible wavelengths and display a significantly bluer spectrum. They do not exhibit significant changes over a period of a few weeks. All these observations are consistent with exposure of water ice at the surface of boulders produced by dislocation of the weakly consolidated layers that cover large areas of the nucleus. Laboratory experiments show that under simulated comet surface conditions, analog samples acquire a vertical stratification with an uppermost porous mantle of refractory dust overlaying a layer of hard ice formed by recondensation or sintering under the insulating dust mantle. The evolution of the visible spectrophotometric properties of samples during sublimation is consistent with the contrasts of brightness and color seen at the surface of the nucleus. Clustered bright spots are formed by the collapse of overhangs that is triggered by mass wasting of deeper layers. Isolated spots might be the result of the emission of boulders at low velocity that are redeposited in other regions.

Key words. comets: general – techniques: image processing – methods: laboratory: solid state

1. Introduction

All cometary nuclei observed so far from spacecraft or ground-based telescopes show a very low visible albedo, in the range of 2 to 5 percent (Lamy et al. 2004; Barucci et al. 2011). Although the close subsurface of the nucleus must be rich in ices to account for the observed gas emissions as the nucleus comes into the vicinity of the Sun, the volatile component is strongly depleted at the surface due to sublimation. As a result, the uppermost layer of the nucleus, which interacts with solar radiation, is essentially composed of refractory organic and mineral matter. Two mechanisms can be involved in the production of this surface mantle: persistence of a sublimation lag after the ice has sublimated and/or accumulation of dust lifted up from the surface by gas drag that was then redeposited at a distant location (Thomas et al. 2015a,b; Davidsson et al. 2015).

Although the surfaces of the comet nuclei visited so far are relatively homogeneous, some of them still show some significant variability in their surface albedo and spectral properties. This is the case in particular of the nucleus of comet 9P/Tempel 1, which displays regions about 30% brighter than surrounding areas at visible wavelengths (Li et al. 2007, 2013). Correlation of visible images and infrared spectra obtained by

the imagers and spectrometers of the Deep Impact spacecraft showed that the brighter areas also display subtle spectral signatures of H₂O ice at 1.5 and 2.0 μm. Modeling of these absorptions indicates 3 to 6% of H₂O ice agglomerates at the surface with diameters between 10 and 50 μm (Sunshine et al. 2006). Observations of the nucleus of comet 103P/Hartley 2 by the same instruments also revealed regions of the nucleus with a reflectance of about twice the average reflectance of the surface, associated with a bluer visible slope (Li et al. 2013). By comparison with what has been observed on 9P/Tempel 1, these observations are also indicative of the presence of H₂O ice at the surface in these regions (Sunshine et al. 2012).

Until the recent in situ investigations of the surface of 67P/Churyumov-Gerasimenko (hereafter 67P) by the Philae lander of the Rosetta mission, the physical properties of the upper desiccated layer that covers most of the nucleus surface could only be inferred indirectly by interpreting remote-sensing data or from experimental results and theoretical considerations. Experiments in space simulators using analog material, in particular those performed at the Deutsches Zentrum für Luft- und Raumfahrt (DLR) of Cologne in the 1980s ("Kometensimulation" KOSI program; Gruen et al. 1991) and at the Institut für Weltraumforschung (IWF) of Graz in the 1990s

(Kömle et al. 1996) have provided quantities of information on the structure of the uppermost layer of the nucleus and the physical processes that affect this layer. Exposed to vacuum and low temperature, mixtures of volatiles and refractory dust evolve rapidly to form stratified samples with a fully desiccated uppermost layer from which grains are regularly ejected, overlaying an ice-rich interior in which the ice has evolved by recondensation and sintering. These evolutions have strong effects on the mechanical, thermal, and spectrophotometric properties of the samples. However, as explained by Keller & Markiewicz (1991), performing a real simulation of a comet surface on Earth is impossible, and the application of laboratory results to the case of a real comet is never straightforward.

More recently, a few groups have initiated new experiments in which analogs for cometary material are exposed to low-temperature and low-pressure environments, focusing on a few particular points that were not directly or fully addressed in previous experiment campaigns. Gundlach et al. (2011) studied the effect of mineral dust on the sublimation to derive the sublimation coefficient of water ice in the presence of impurities. Kossacki & Leliwa-Kopystynski (2014) showed that even small amounts of dissolved minerals mixed within the ice affect the temperature dependence of its sublimation coefficient. Brown et al. (2012) and Moores et al. (2012) studied how contaminants in the water ice affect the isotopic composition of the water vapor emitted from dusty samples during long-duration (up to 35 days) sublimation experiments. The Laboratory for Outflow Studies of Sublimating materials (LOSSy) has been set up at the University of Bern with the aim to characterize the visible spectrophotometric properties of analogs of solar system icy surfaces with a special emphasis on comets (Pommerol et al. 2011, 2015; Poch et al. 2015). New sublimation experiments have been undertaken using modern digital imaging techniques to characterize simultaneously and in situ the evolution of the texture and spectrophotometric properties of the surface of various samples exposed to vacuum and low temperature for durations of a few tens of hours. The results of these various experiments are used here to interpret some of the most intriguing observations of comet 67P by the scientific camera onboard Rosetta.

Since the acquisition of the first resolved image of the nucleus of comet 67P in June 2014, the Optical, Spectroscopic, and Infrared Remote Imaging System (OSIRIS), the Narrow Angle Camera (NAC), and the Wide Angle Camera (WAC) onboard ESA's Rosetta spacecraft (Keller et al. 2007) have scrutinized the surface under changing illumination conditions, variable spatial resolution, and in different wavelength bands, producing the most detailed atlas yet of a comet nucleus surface. Global color images of the nucleus reveal a generally dark (geometric albedo of 5.9% at 550 nm, Sierks et al. 2015), red (red slope of 11%/(100 nm) at 1.3° phase angle), and homogeneous surface with the exception of the Hapi region, which displays a slightly higher reflectance (by 16%) and is notably bluer (red slope 50% less steep) than the rest of the surface (Fornasier et al. 2015, Fig. 6). Similarities with the bright and blue H_2O ice-bearing regions on Tempel 1 and Hartey 2 might indicate the possible presence of a small fraction of H_2O ice mixed with refractory material at the surface of Hapi, an interpretation tentatively confirmed by the Visual, Infrared and Thermal Imaging Spectrometer (VIRTIS; Capaccioni et al. 2015). The surface is strongly backscattering (i.e., the surface reflectance decreases nonlinearly by a factor of 5 as the phase angle increases from 0 to 60°) and shows a significant phase reddening (i.e., the visible red slope increases from 11 to 16%/(100 nm) as the phase angle increases from 0 to 60°; Fornasier et al. 2015, Sect. 3.3).

At a small scale however, the surface is much more heterogeneous. As the spatial resolution of the images was increasing from June to October 2014, more and more variability at the smallest resolved scale could be observed in the form of isolated or clustered bright spots with a strong contrast of the albedo compared to the surrounding surfaces and a distinctive bluer color. In this article, we analyze the properties of these small bright features as observed by OSIRIS until early November 2014, before Philae separation and landing, and we interpret them by means of comparisons with the results of past and recent laboratory experiments.

Section 2 is devoted to the description of the bright features, as they appear in OSIRIS NAC images. They are classified according to their morphology and the regions of the nucleus in which they are observed. We compare images of given features acquired at different times to assess their potential temporal variability. Their relative reflectance through the different NAC filters is derived, and false-color images and reflectance spectra are generated. We conclude that the bright spots are exposures of dirty H_2O ice. Section 3 presents interpretations of the results of recent comet laboratory experiments (Pommerol et al. 2015; Poch et al. 2015) as well as a summary of past results, which are particularly relevant for the understanding of the nature and origin of the bright features observed at the surface of the nucleus of 67P. The comparison between the OSIRIS observations and results of laboratory experiments is further detailed in Sect. 4 where implications regarding the nature and origin of the bright spots observed at the surface of 67P are proposed. Section 5 summarizes this discussion and lists our main conclusions.

2. OSIRIS observations

2.1. Data and methods

As most of the features studied in this article are only a few meters wide, we have restricted our analysis to the data of the Narrow Angle Camera (NAC), a framing camera of 2048×2048 pixels with 18.6 μrad/pixel angular resolution and a 2.2° field of view (Keller et al. 2007). Two filter wheels in front of the detector are used to switch between bandpass filters and acquire series of monochrome images in up to 11 different wavelengths from the ultraviolet (269 nm) to the near-infrared (989 nm). Because of the time needed to switch filters and trigger a new image acquisition, the different images of a color series are taken at intervals of time of about 15 s. As the comet rotates and the spacecraft moves onto its trajectory during this time, it is necessary to first coregister the images acquired through the different filters to produce a multispectral cube from which color images can be produced and reflectance spectra extracted.

We used images acquired between the beginning of August 2014 (arrival of Rosetta at the comet) and the beginning of November 2014 (release of Philae). The average distance from the spacecraft to the surface decreased by steps from 125 km in August to 10 km in October. As a result, the resolution of the images varies from about 2 m to 0.17 m/pixel. The heliocentric distance decreased from 3.6 to 3.0 AU during this period of time. The coverage of the surface during this mapping phase is not homogeneous, some regions having been imaged more frequently than others. The illumination conditions also show extreme variations across the surface, of which 30% was still permanently shadowed and had never been observed during the mapping phase. A high-resolution and accurate digital terrain model (DTM) is thus crucial to retrieve absolute values of

reflectance from the images. The phase angle is also highly variable among images; it varies between 35° and 115° for the subset of the NAC dataset used in this work. Data were calibrated through the standard OSIRIS calibration pipeline (Tubiana et al. 2015). We used here the level 3 images, calibrated into spectral radiance units [W m^{-2} Sr^{-1} nm^{-1}].

To establish a catalog of the bright features at the surface of the nucleus, we have visually inspected all NAC images acquired through the orange filter (649.2 nm), which is the filter most often used for surface mapping. We looked for small features with high brightness that could not obviously be explained by local topography and illumination effects. The main difficulty at this stage was to distinguish small bright features at the surface from the effect of cosmic rays hitting the detector. We adopted a two-step process, in which we first selected all bright features regardless of their possible origin, and in a second step identified the features that certainly were surface features. This distinction was made on the basis of multiple observations of the same features in different images, observation of the shape and brightness of the bright feature at full scale, and/or identification of the feature in the different color frames in the case where images were acquired through different filters.

In the absence of a global coordinate system for the mapping of the surface of 67P, we recorded the locations of the bright features by saving the pixel coordinates of rectangular sub-frames and systematically identified the regions in which the features were observed, following the up-to-date definitions of El-Maarry et al. (2015). The pixel scales of all images were calculated using the SPICE toolkit and mission kernels provided by ESA. We note that these pixel scales are estimated for a calculated distance of the spacecraft to the center of the comet and do not take into account the distance of the surface to the center. Therefore, a relative uncertainty in the range of a few percent for the most distant observations and up to 20% for the closest observations must be considered for all scale bars shown in this article.

The heliocentric distance of 67P at the time of imaging was calculated with the SPICE toolkit as well. This value was used to compute the surface reflectance by scaling the reference solar spectral irradiance measured at the top of Earth's atmosphere to the current heliocentric distance. A major difficulty in deriving the reflectance factor of small surface features is the determination of the local incidence angle, which requires an accurate DTM. We used here the most resolved DTM available within the OSIRIS team at the time of this analysis, which contains 5899067 vertices with an average resolution of 2 m/pixel. Using this DTM together with orbit information from SPICE and a 3D visualization engine, we calculated maps of the incidence and emission angles, which are used for first-order estimations of the local solar irradiance and hence surface reflectance. Unfortunately, the limited spatial resolution of the DTM results in large uncertainties on the derivation of reflectance factor values from radiance factor values.

Accurately coregistering images acquired through the different filters is a challenging task because of the rapid relative movements of Rosetta above the surface. To simplify the problem, we only coregistered small subframes, a few hundred pixels wide, that contained the bright features. In that case and if the surface topography inside the subframe was negligible, it became possible to use automatic subpixel cross-correlation algorithms based on a Fourier transform of the image. This technique was used for all images of a color sequence to produce a multispectral cube. Regions of interest (ROI) were then defined manually to select the central pixels belonging to a given bright feature while avoiding pixels at the periphery that might

be affected by imperfect coregistration. The average reflectance of the bright feature at the different wavelengths and its standard deviation were then calculated and compared to the reflectance of the surrounding terrain estimated by using the same technique. Spectral ratios were then produced to isolate the spectral characteristics of the bright features. The red slope was calculated between wavelengths 535.7 and 882.1 nm and normalized by the value of reflectance at 535.7 nm, following the definition proposed by Fornasier et al. (2015), Sect. 3.3. We note that different combinations of filters have been used at different times of the mapping phase as a result of operational limitations. This is the reason why the spectra and spectral ratios presented in this article do not always have the same numbers of points and the same wavelengths. Images acquired through the filters centered at 701.2 nm and 743.7 nm seem to be affected by a coma emission, presumably H$_2$O$^+$ and NH$_2$ (Fornasier et al. 2015). The values of surface reflectance derived from these images are thus more uncertain and artifacts on the spectra are often visible at these wavelengths.

2.2. Categories of bright features

Our current catalog of bright features contains 172 observations for a total of about 120 individual surface features, with up to 11 different successive observations. This total does not include the cases of some imaging sequences where the features were rapidly imaged at intervals of time of only a few minutes. Because of the very similar resolution, illumination, and observational conditions, they were considered as single observations.

We classified the observed bright features into three categories: clusters of bright features (more than three bright spots, Figs. 1, 2), isolated bright features (up to three individuals in close vicinity, Fig. 3), and boulders displaying bright patches at their surface (Fig. 4). The four examples of clusters of bright features shown in Fig. 1 are representative of the 18 clusters currently identified at the surface of the nucleus. They consist of up to a few tens of meter-sized boulders spread over a few decameters. They are often observed in the immediate vicinity of decameter-high cliffs in the regions consisting of brittle material (Thomas et al. 2015b; El-Maarry et al. 2015, Table 1). Some of the clusters of bright features observed here seem to be a particular case of boulder clusters identified at many places over the nucleus and studied in detail by Pajola et al. (2015). The large majority of these boulder clusters do not show any contrast of brightness with the surrounding terrains; bright clusters seem to be an exception.

For five of the about twenty bright clusters identified at the surface of the nucleus, we counted and measured the diameters of the bright spots following the definitions and methods presented in detail by Pajola et al. (2015), Sect. 3, to derive their cumulative size-frequency distribution. The main goal of this statistical analysis is to compare the diameter distributions of the bright boulders with those derived for the numerous boulder clusters located across the surface of 67P, which do not display any particular color or brightness variability.

The specific areas analyzed are presented together with the boulder classification and location in Fig. 2. Clusters 1, 2, 3, and 5 are all located in the immediate vicinity of decameter-high cliffs, whereas cluster 4 is located in a different geomorphologic setting, on the wall of a cliff. For each of the clusters, we computed the cumulative size-frequency distribution by taking into consideration only the boulder diameters that satisfy the three-pixel sampling rule to be quite sure of their extraction
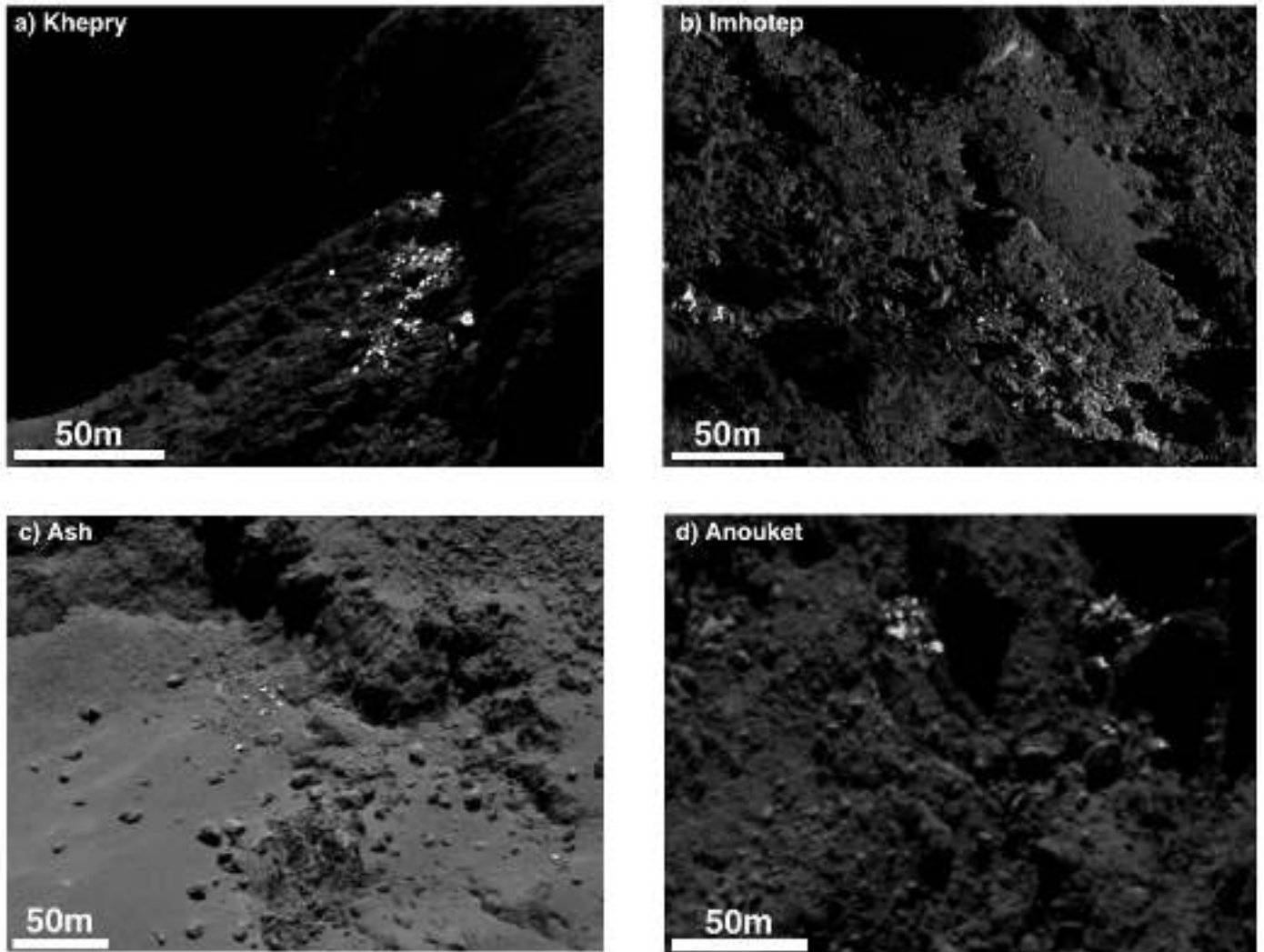
Fig. 1. Examples of clusters of bright spots observed in four different regions of the comet: **a)** Khepry; **b)** Imhotep; **c)** Ash; and **d)** Anouket. Clusters of bright spots are frequently observed in debris fields in the vicinity of decameter-high cliffs. They are generally found in areas receiving low insulation, as suggested by the amount of shadow in the images. **a)** Khepry. Subset of OSIRIS NAC image: NAC_2014-09-30T04.43.14.587Z_ID30_1397549100_F22.IMG; **b)** Imhotep. Subset of OSIRIS NAC image: NAC_2014-09-30T01.23.46.579Z_ID30_1397549100_F22.IMG; **c)** Ash. Subset of OSIRIS NAC image: NAC_2014-09-19T18.34.00.344Z_ID30_1397549800_F22.IMG; **d)** Anouket. Subset of OSIRIS NAC image: NAC_2014-09-16T09.43.48.370Z_ID30_1397549200_F22.IMG.

(Pajola et al. 2015, Sect. 3). Depending on the resolution of the images, these values are between 1 and 2 m. Nevertheless, Fig. 2 shows that even smaller boulders with dimensions between 0.7 and 1.5 m have been identified, thanks to shadows on the surface favored by the phase angle of the observations. However, these bright boulders have not been taken into account in the power-law fit since they are not statistically significant.

The power-law indices derived from the fits are shown in Fig. 2. Clusters 1, 2, 3, and 5 (Figs. 2a–c, and e) display similar trends and are entirely superimposed when the measured error bars are taken into consideration; in contrast, cluster 4 (Fig. 2d) can be considered as an outlier, since the measured slope is different from that of the others. The meaning of the power-law indices derived here and their general behavior are discussed in detail in Sect. 4.

Isolated bright spots can be observed in all types of regions. Figures 3a–d all show bright spots over the consolidated fractured material observed in many other regions of the nucleus, whereas Fig. 3b shows an example of a bright spot lying at the surface of the smooth dust unit that covers large areas of

the Ash region. The relation between these bright spots and the surrounding terrain is generally unclear. In some cases, such as Fig. 3d, the bright spot seems to be part of the unit over which it appears. In other cases, such as Fig. 3b, there is no evidence of a structural relation between the bright particle and the local unit.

Boulders displaying bright patches at their surface (Fig. 4) are observed both as clusters and isolated. The shape of the bright patches visible on their surfaces is relatively variable, often consisting of some circular bright spots and/or stripes, generally around the periphery (Figs. 4a–c). In general, most of the surface shows a reflectance similar to the surrounding terrain, and the bright fraction only occupies a minor part of the boulder's surface. As illustrated in Fig. 5, it seems that many of the clustered and isolated bright spots seen at low resolution also consist of boulders with bright patches when observed at higher resolution. It is thus possible that this is a general characteristics of all the bright spots, although this cannot be proven because of the limited resolution of some observations. In that case, the typical size of the bright spots determined from the highest resolution observations would be of about one to two meters, smaller
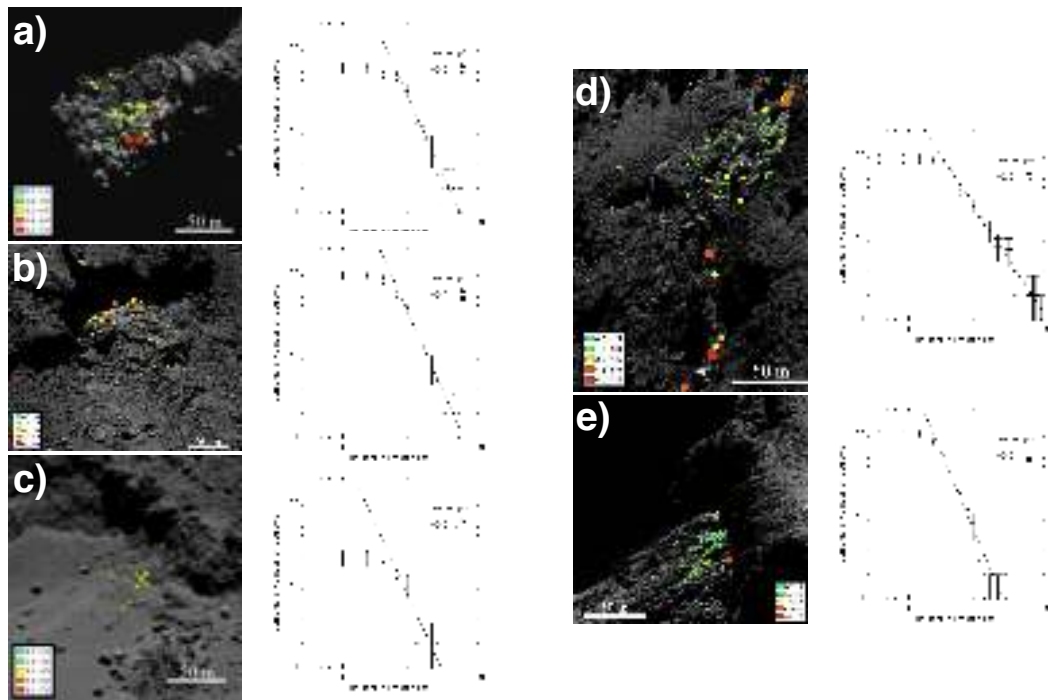
Fig. 2. Cumulative size-frequency distributions for five clusters of bright features. Boulders with a dimension greater than one to two meters have been considered for these distributions, depending on the resolution of these images. The index of the power-law distribution fitted on the data is indicated in each plot.

by a factor of five than what could be inferred from the initial lower resolution observations.

Profiles of the radiance factor at 649.2 nm extracted from the images show that the bright spots can be up to ten times brighter than the average reflectance of the surrounding terrains, as illustrated in Fig. 6 for the cases of features shown in Figs. 1a and 7a. First-order conversion to reflectance factor using local incidence angles calculated from the DTM indicates a reflectance of about 0.13 for the bright spots in both cases, whereas the reflectance factor of the dark surrounding terrain is in the 0.01 to 0.02 range. These images have been acquired at high phase angles, 57.7° and 92.3°, respectively, and the reflectance factors obtained here are much lower than the values of I/F derived from observations at near-0° phase angle because of the steepness of the surface phase curve (Fornasier et al. 2015, Sect. 3.1).

2.3. Temporal evolution of the bright regions

Detecting possible temporal variability of the observed bright features is one of the most important parts in analyzing them because this provides indications about their composition. However, this proved to be extremely challenging because illumination and observation geometry as well as variable resolution continuously changed. Figure 7 shows three bright features in three different regions, each observed three times with the same orange filter. Some images are separated by two weeks, while others were only acquired a few hours apart. In addition, the image shown in Fig. 1a shows the same feature as Fig. 7b at a later time (30.09). In these three cases, a quick comparison of the first two images of the time series might lead to the conclusion that some surface changes occurred, either by disappearance or appearance of small bright dots or by a change in the shape of the

bright feature. However, comparison with the third image of the time series, acquired in conditions of illumination and observation relatively similar to the first image, shows that all the apparent changes were only due to differences in the illumination conditions.

Difficulties in analyzing temporal changes of the bright surface features are inherently related to their location in the areas of the surface that receives the lowest insolation. The high surface roughness and high incidence angles result in long shadows that cover a large part of the images. The length and direction of the shadows changes rapidly with the local time and complicates the comparison of images. This is particularly crucial for bright features that are completely surrounded by shadows, such as the one shown in Fig. 7a. Moreover, the contrast of reflectance between the bright features and the surrounding dark terrains is also likely to change with emission and phase angle. Finally, the differences of resolution complicate the situation ever more because, as detailed in Sect. 2.2 and Fig. 5, increasing the resolution often allows us to distinguish previously unresolved bright patches on surfaces that looked homogeneous at lower resolution.

Keeping in mind all these possible effects and analyzing the images available at the highest level of detail possible, we did not detect any evidence for temporal changes in the dataset so far.

2.4. Colors

Images through different color filters have been acquired for about 50% of the individual bright features identified at the surface. The other 50% have only been imaged through the orange filter (649.2 nm). Multispectral cubes of small subsets of the full frames were assembled and used to produce RGB color composites and extract reflectance spectra, as detailed in Sect. 2.1. False-color RGB images of various bright features assembled from
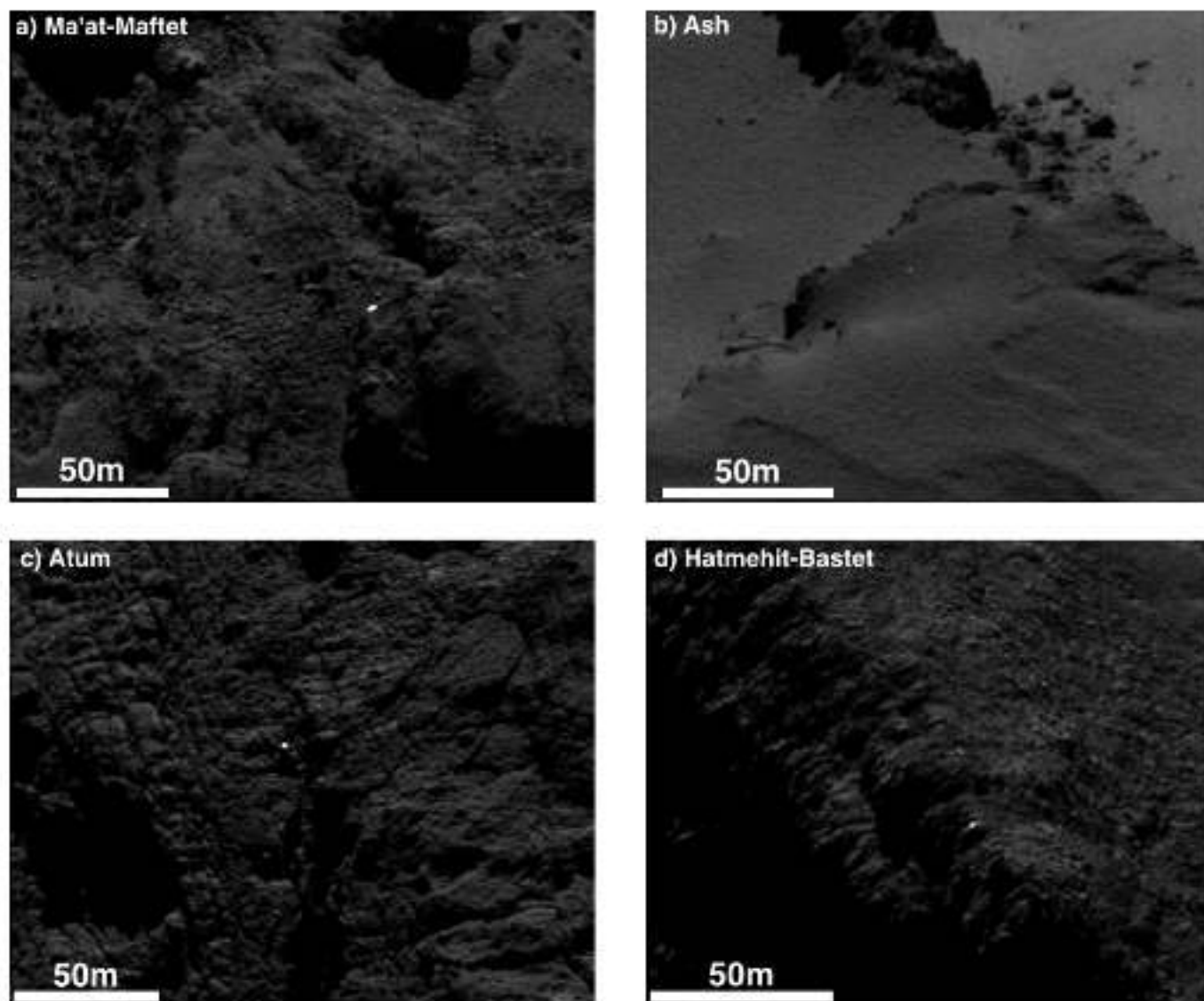
Fig. 3. Examples of isolated bright spots observed in four different regions of the comet: **a)** boundary between Ma'at and Maftet; **b)** Ash; and **c)** Atum; **d)** boundary between Hatmehit and Bastet. While the examples shown in **a)**, **c)**, and **d)** are all inside regions consisting of consolidated material; **b)** shows the example of an isolated bright spot lying in the smooth dusty terrain that covers the region of Ash. **a)** Ma'at-Maftet. Subset of OSIRIS NAC image: NAC_2014-10-05T23.54.02.593Z_ID30_1397549500_F22.IMG; **b)** Ash. Subset of OSIRIS NAC image: NAC_2014-10-03T23.22.22.559Z_ID30_1397549500_F22.IMG; **c)** Atum. Subset of OSIRIS NAC image: NAC_2014-10-04T19.16.24.527Z_ID30_1397549500_F22.IMG; **d)** Hatmehit-Bastet: NAC_2014-10-04T19.16.24.527Z_ID30_1397549500_F22.IMG.

monochrome images acquired at near-infrared, visible, and near-ultraviolet wavelengths, respectively, are shown in Fig. 8. Each of the three color channels, 882.1 nm, 649.2 nm, and 360.0 nm for the R, G, and B channel, respectively, was independently stretched and slightly saturated to emphasize the contrasts of color across the scene. This reveals significant contrast of color between dark terrains displaying a redder color and bright features displaying a significantly bluer color. Red slope images (not shown) were produced as well, from the images acquired at 535.7 and 882.1 nm, which clearly distinguish the bright features as areas of very low red slope.

These differences in color observed in RGB images are better described quantitatively by extracting average reflectance spectra over regions of interest and by calculating spectral ratios between the bright features and the dark surrounding terrains. As shown in Fig. 9 and presented in detail by Fornasier et al. (2015),

Sect. 3.2, the reflectance spectrum of most of the surface of 67P shows a nearly linear red slope over the 300–1000 nm spectral range, the reflectance at 1000 nm being two to three times higher than at 300 nm. If most of the bright features also show a red slope over this spectral range, the steepness of this red slope is considerably reduced, resulting in a bluer spectrum. The spectral ratio calculated between the bright features and the darker surrounding terrain systematically displays a linear blue slope, as shown by the linear fits plotted over the measured points in Fig. 9.

The exposure of H_2O ice at the surface of boulders is the most plausible scenario to explain the occurrence and properties of the bright features at the surface of the comet. Various ices, H_2O, CO_2, and CO would be consistent with both the brightness and color of the bright spots when mixed with dust. However, water ice is the strongest candidate considering that we have not
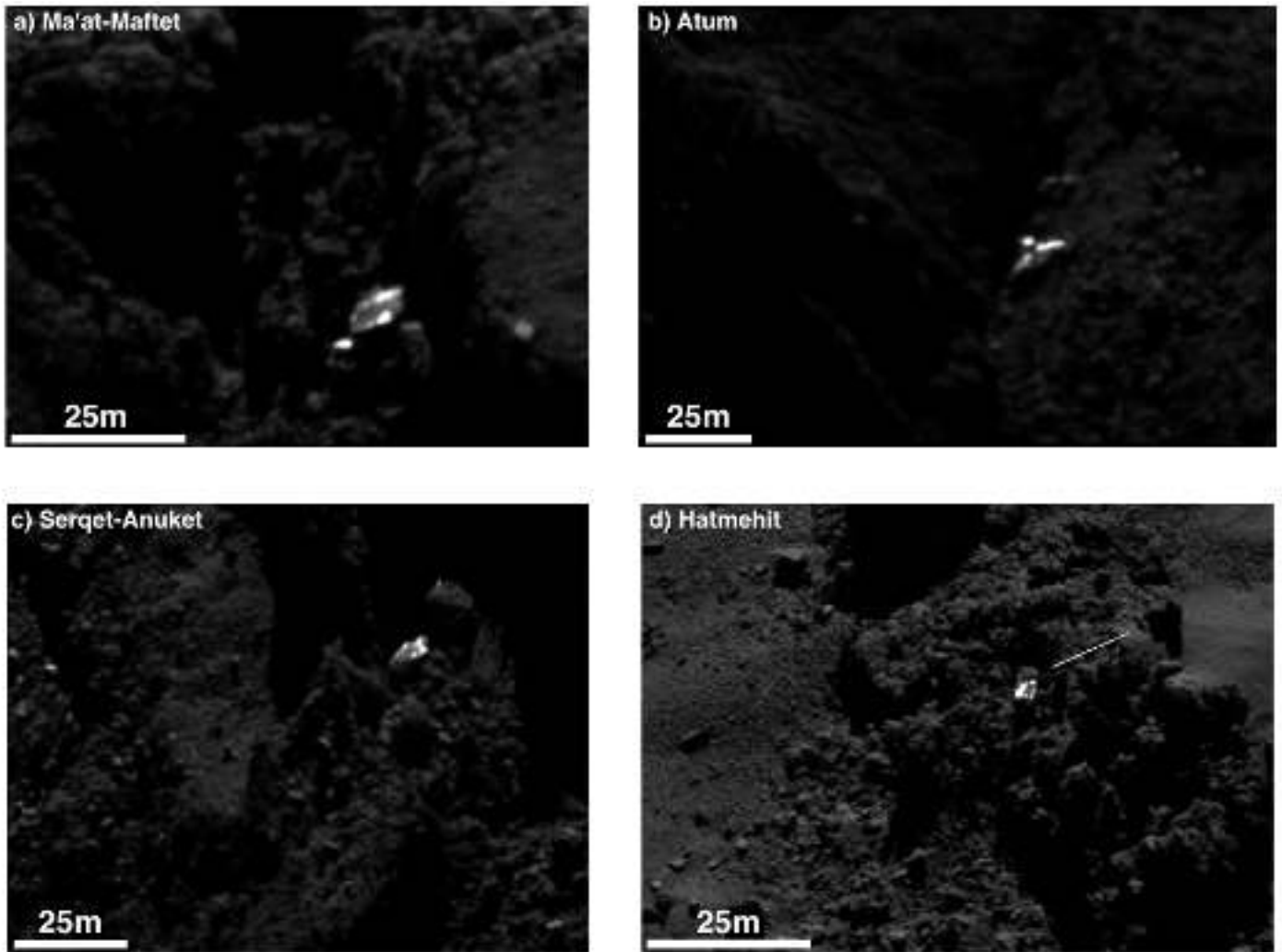
Fig. 4. Examples of boulders displaying bright patches on their surface in four different regions of the comet: **a)** boundary between Ma'at and Maftet; **b)** Atum; **c)** boundary between Serqet and Anuket; **d)** Hatmehit. These boulders are about 10 m long. The bright spots are typically one to two meters in diameter. The bright stripes in images a) and b) are also about one to two meters wide. **a)** Ma'at-Maftet. Subset of OSIRIS NAC image: NAC_2014-10-05T23.54.02.593Z_ID30_1397549500_F22.IMG; **b)** Atum. Subset of OSIRIS NAC image: NAC_2014-11-03T12.17.55.805Z_ID30_1397549000_F22.IMG; **c)** Serqet-Anuket. Subset of OSIRIS NAC image: NAC_2014-09-29T07.12.53.553Z_ID30_1397549400_F22.IMG; **d)** Hatmehit. Subset of OSIRIS NAC image: NAC_2014-09-30T20.44.47.569Z_ID30_1397549300_F22.IMG.

observed any obvious temporal evolution (Sect. 2.3). Indeed, as detailed in Sect. 4, the sublimation rate of H$_2$O ice at a heliocentric distance of 3.5 AU is lower than one millimeter per hour, whereas CO$_2$ or CO would very rapidly disappear when directly illuminated. This hypothesis is explored and refined in more detail below.

3. Insights from laboratory experiments

The KOSI experiments conducted at the DLR in the 1980s have provided a multitude of information on the behavior of H$_2$O and CO$_2$ ices mixed with mineral contaminants under simulated comet surface conditions. Cross-sections of the various samples after a few hours of irradiation by simulated solar light show a strong vertical stratification of the samples. Of particular significance for interpreting the OSIRIS results we present here are the uppermost layer of pure dust, which was observed to reach a thickness of 1 to 2 mm, and immediately below a hard crust of variable thickness formed by sintering of the ice and/or recondensation of sublimated water vapour. A 1 millimeter-thick layer of dark fine-grained dust is sufficient to absorb and scatter all incident visible photons and hide all layers underneath from optical instruments.

The formation of a centimeter-thick layer of hard sintered ice below the uppermost dust layer has important implications for the mechanical behavior of the surface, as shown by Seiferlin et al. (1995) , who reported a compressive strength of the hard ice layer that is one order of magnitude higher than the initial granular material. This certainly also has consequences for the spectrophotometry because the sintering or recondensation of the ice may result in the segregation of the ice and dust components. If they were initially well mixed, even a very small amount of fine organic-rich dust would be sufficient to decrease the albedo of the ice to values of a few percent. However, if the evolution of the material results in a spatial segregation of the dust and the ice, the albedo will increase significantly.

Kömle et al. (1996) and Kossacki et al. (1997) have conducted experiments at the Institut für Weltraumforschung (IWF) of Graz to complement previous KOSI studies, largely reusing similar protocols and materials. Kömle et al. (1996) introduced
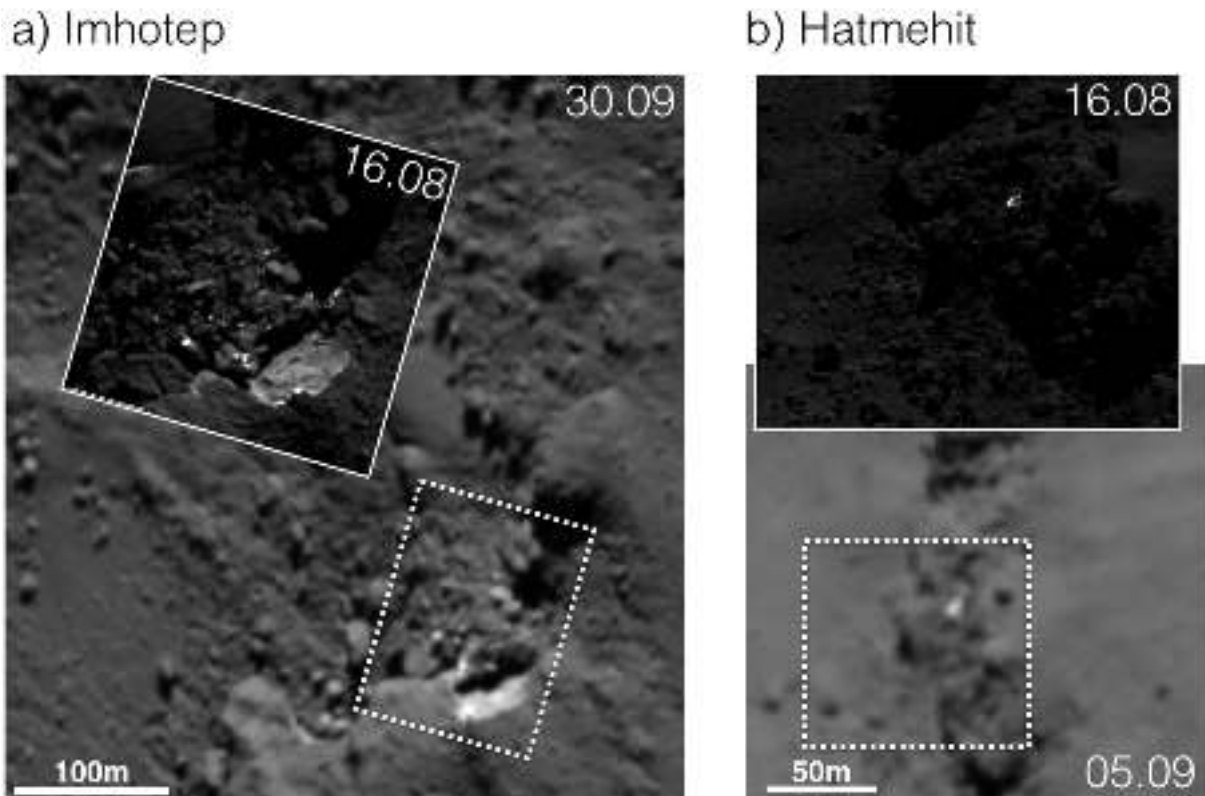
Fig. 5. Effect of the spatial resolution on the aspect of surface bright features. In both examples shown here, the surface shown at higher resolution allows resolving small meter-sized bright spots inside what looks like homogeneous bright regions at lower scale. As a result, the bright spots are much smaller and brighter than what could be inferred from the earlier lower resolution observation. **a)** Imhotep. Subset of OSIRIS NAC images: NAC_2014-08-16T19.59.14.556Z_ID30_1397549300_F22.IMG NAC_2014-09-30T20.44.47.569Z_ID30_1397549300_F22.IMG; **b)** Hatmehit. Subset of OSIRIS NAC images: NAC_2014-08-16T15.59.14.568Z_ID30_1397549500_F22.IMG NAC_2014-09-05T08.00.55.651Z_ID30_1397549500_F22.IMG.

paraffin in the ice-dust mixture to simulate the organic component inferred at the surface of comets. They observed that in addition to the hard icy layer formed by sintering or recondensation of ice, a cohesive ice-free crust had been formed by the paraffin, which acted as a glue between mineral grains. The results of Kossacki et al. (1997) showed that the thickness of the hard ice layer below the surface can reach the entire thickness of the sample holder, 8 cm in that case, after a few tens of hours of insolation. Depending on the exact physical process at work in the metamorphism of the ice layer, it might show a higher bulk density than the initial highly porous material. It is also possible, however, that the texture of the ice evolves by sintering with formation of bonds between ice grains, without affecting its bulk density. In any case, the structural changes have strong positive effects on the thermal conductivity. The layer of hard recondensed or sintered ice is thus more efficient in transporting heat to the subsurface. However, the millimeter-thick layer of dust formed at the surface is extremely insulating and will restrict the solar heat conduction to depth. If the series of experiments performed in the 1980 s in Cologne and in the 1990 s in Graz provide insightful information about the structure, mechanical and thermal properties of the surface of the nucleus, they are of limited interest for our understanding of the spectrophotometry of the surface, which is dominated by the absorption of dark organic material.

New sublimation experiments have recently been undertaken at the University of Bern with a clear focus on the spectrophotometric properties of the surface of the sample during its sublimation. The SCITEAS simulation chamber (Pommerol et al. 2015),

designed and constructed for that purpose, is equipped with a large window that permits the acquisition of visible and near-infrared hyperspectral cubes of the surface of a sample placed under secondary vacuum and kept at temperatures below the free sublimation temperature of H_2O ice. It complements the PHIRE-2 gonio-radiometer, which is used to measure the bidirectional visible reflectance of samples over wide ranges of incidence, emission, and phase angles.

The samples consist of spherical particles of H_2O ice produced in two different particle size fractions with average diameters of 6 ± 3 and $70 \pm 30\,\mu$m, respectively, mixed with different types of dark and colored minerals and organics compounds. For the mineral component, volcanic airfall ash of basaltic composition is used (JSC-1AF simulant, Owens 2006), as well as olivine and smectite clay. For the organic component, nanoparticles of carbon black as well as tholins produced from gas-phase reactions between CH_4 and N_2 (Carrasco et al. 2009) are used. Beyond the choice of the individual components, a key question when producing analogs for cometary material is the mixing mode between the ice and the contaminants. Various properties of the material will be very different if grains of pure ice are intimately mixed with grains of pure mineral and organic matter or if the particles of refractory contaminants are embedded into larger particles of ice. Both mixing modes were thus used and results compared, whenever this was possible.

The various experiments conducted with the SCITEAS facility and different samples show common trends and similarities to previous experimental results as well as some variability of behavior (Pommerol et al. 2015; Poch et al. 2015). The

a) Imhotep

Incidence angle: 55°
Phase angle: 57.7°

b) Khepry

Incidence angle: 70°
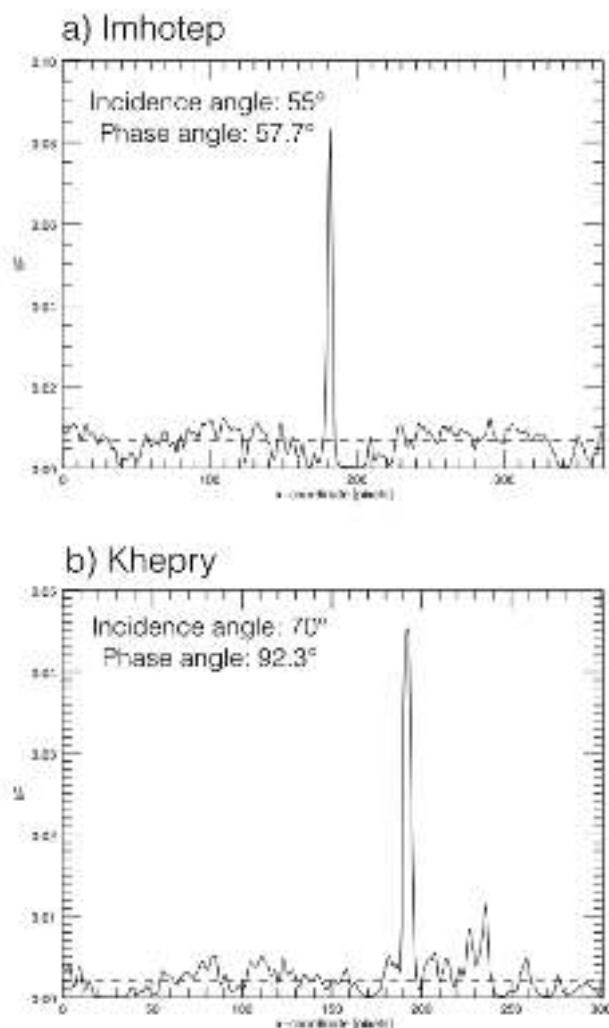Phase angle: 92.3°

Fig. 6. Profiles of radiance factor I/F through two different bright features: **a)** bright field shown in Fig. 1a. **b)** Bright feature shown in Fig. 6a. The average incidence angles estimated from the DTM are 55° and 70°, respectively. This gives multiplication factors of 1.74 and 2.92, respectively, to calculate the reflectance factors, which reach about 0.13 in both cases over the brightest spots.

development of a layer of dust at the surface during the first hours of the experiments was observed for all samples. However, its structure, porosity, thickness, reflectance, and color are highly dependent on the nature and amount of the contaminant as well as on its mixing mode with the ice. The ejection of large grains or even centimeter-sized chunks of the uppermost mantle is observed, sometimes multiple times, for some samples. Of particular interest are the repeated ejections of large (>cm) but thin (<mm) fragments of a very high porosity (>90%) mantle made of tholins, which indicates very high cohesion within the mantle but low cohesion between the mantle and the icy material underneath. An example of such a mantle and ejected fragments is shown in Fig. 10 in a sublimating sample of water ice particles into which tholins have been embedded (intra-mixture). The freshly exposed water ice particles (area A in Fig. 10) appear significantly brighter and less red than the surrounding water-free mantle of tholins. We also observed the formation of hard layers of sintered ice below the dust in some of our experiments. Interestingly, it seems that the mixing mode of the ice with the impurities plays a major role in the formation of this layer. We

see the formation of a hard ice crust when the ice and impurities were previously intimately mixed at the grain level (inter-mixture). When the mineral and organic particles were initially embedded in the grains of ice (intra-mixture) and for the same ice-to-dust ratio, no formation of hard ice crust was observed.

In all experiments, we see a fast darkening of the surface during the first hours as the water ice sublimes from the surface and the dust mantle forms. In some cases, the mantle eventually becomes optically thick, completely hiding the icy material below. In other cases, chunks of the mantle are regularly ejected or grains move across the surface so that new parts of the underlying icy material are continuously exposed. Interestingly, because of the extremely high porosity of the cohesive mantle formed with some materials, the spectrophotometric properties of this mantle can be quite different from those of the pure compound measured in a granular higher density state. The comet #1 experiment, detailed in Pommerol et al. (2015), is particularly relevant for this study as the reflectance level of the dust mantle is relatively similar to the average reflectance at visible wavelengths measured at the surface of 67P. Such a low albedo was obtained by using 1 wt.% nanoparticles of carbon black as the organic contaminant in H$_2$O ice in addition to 5 wt.% of volcanic airfall ash of basaltic composition. Together with a low albedo, this sample also shows a red slope over the entire 400–1000 nm spectral range, although less steep than the one observed at the surface of 67P.

Normalized reflectance spectra and spectral ratios for two different steps of the sublimation are presented in Fig. 11. The two plots on the left, a) and c), use data acquired at the very beginning and very end of the sublimation experiment and as a result show a high contrast of albedo. The two plots on the right of Figs. 11, b) and d), use the same data for the final state of the sample but a later stage of the evolution for the other state. In both cases, the ratios between the spectra of the bright and dark sample show a linear blue slope over the entire spectral range. The linear blue slope seems to be slightly affected by a very shallow and broad absorption band centered at 800 μm, probably due to the Fe^{2+}–Fe^{3+} charge transfer absorption band of the pyroxenes contained in the volcanic ash.

Although the general behavior seen at the surface of the comet is well reproduced in laboratory experiments in the form of the blue linear slope in spectral ratios, one can see a significant discrepancy in the magnitude of the red slope of the non icy component and hence in the magnitude of the linear blue slope. The red slope seems steeper by a factor of two at the surface of 67P than in the particular laboratory experiment analyzed here. There are two main reasons for this discrepancy. First, the relatively strong phase reddening observed at the surface of the comet (Fornasier et al. 2015, Sect. 3.3) can be responsible for a large part of the difference. Indeed, observations of the bright spots were acquired at relatively large phase angles, whereas the laboratory data were acquired at a phase angle of about 10°. Second, the organic matter at the surface of the comet probably displays a redder spectrum than the one of the carbon black used in the experiments. When using tholins mixed with water ice in the laboratory experiments (see Fig. 10), one can also observe much steeper red slopes. Future laboratory studies should address this particular point by investigating which compositions of the organic component provide good agreement with the values of red slope observed at the surface of 67P.

In addition to the visible spectral range, reflectance data were also acquired through the near-infrared, up to 2.4 μm. Acquiring data simultaneously in the VIS and NIR spectral ranges for the same sample is useful to understand how the data obtained by

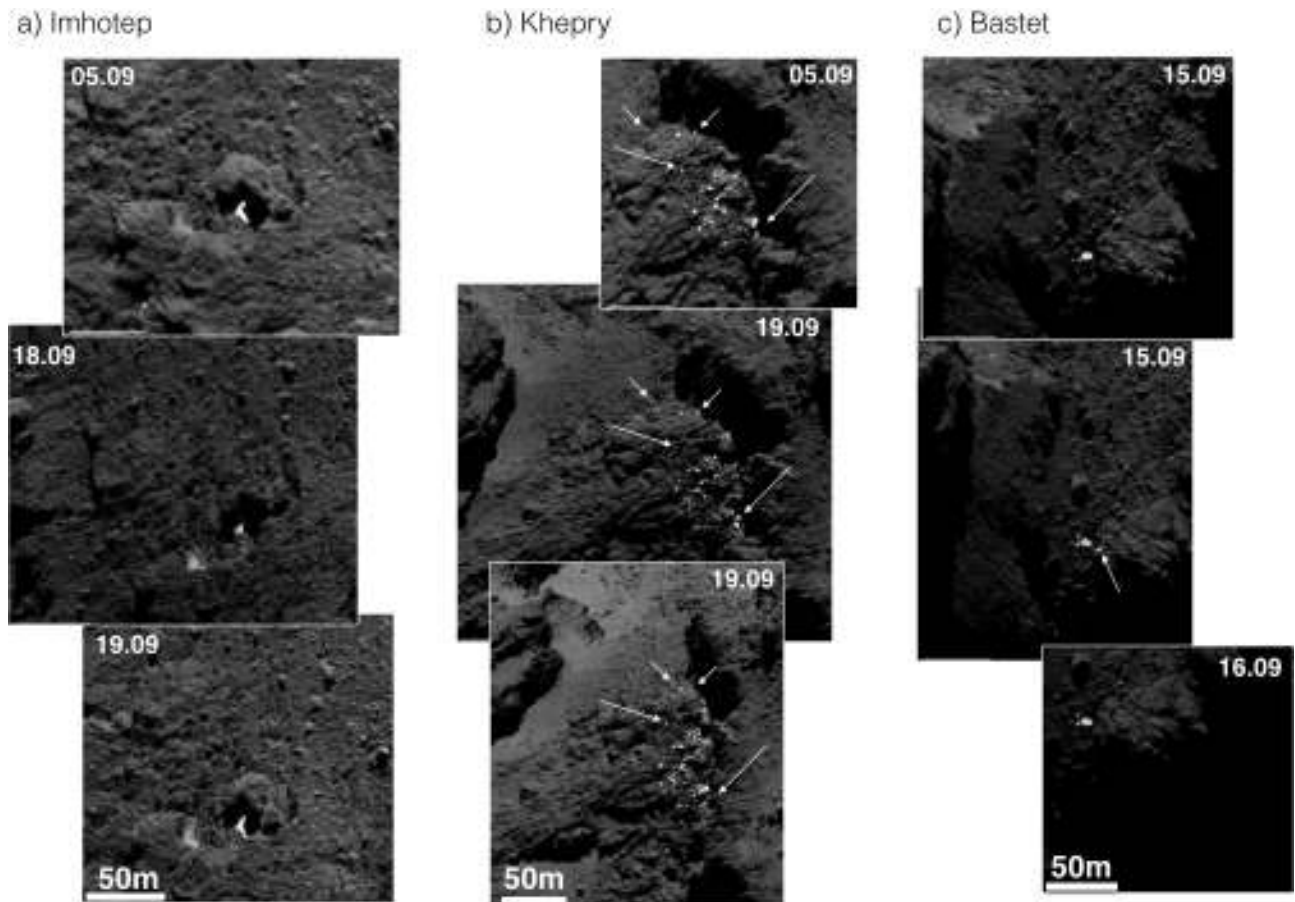a) Imhotep   b) Khepry   c) Bastet

Fig. 7. Comparison of the aspect of three different bright features seen at three different times in the regions of **a)** Imhotep; **b)** Khepry; and **c)** Bastet. The date at which each image was acquired is indicated in an upper corner. **a)** Imhotep. Subsets of OSIRIS NAC images: NAC_2014-09-05T06.35.55.557Z_ID30_1397549300_F22.IMG (phase = 57.7°) NAC_2014-09-18T04.01.49.361Z_ID30_1397549200_F22.IMG (phase = 83.3°) NAC_2014-09-19T05.32.32.380Z_ID30_1397549800_F22.IMG (phase = 70.4°); **b)** Khepry. Subsets of OSIRIS NAC images: NAC_2014-09-05T09.30.55.562Z_ID30_1397549400_F22.IMG (phase = 59.2°) NAC_2014-09-19T09.19.13.330Z_ID30_1397549600_F22.IMG (phase = 70.5°) NAC_2014-09-19T21.03.31.329Z_ID30_1397549000_F22.IMG (phase = 66.4°); **c)** Bastet. Subsets of OSIRIS NAC images: NAC_2014-09-15T05.42.12.353Z_ID30_1397549000_F22.IMG (phase = 67.3°) NAC_2014-09-15T18.46.16.351Z_ID30_1397549600_F22.IMG (phase = 72.6°) NAC_2014-09-16T06.54.55.313Z_ID30_1397549400_F22.IMG (phase = 78.5°).

the OSIRIS camera and by the Visible and Infrared Thermal Imaging Spectrometer (VIRTIS, Coradini et al. 1999) can be compared. The results of this analysis are summarized in Fig. 12 and discussed in Sect. 4.

The sublimation of the water ice itself is not a simplistic process. Experimental studies of its sublimation rate under controlled conditions (Beckmann & Lacmann 1982) have shown that the measured rates differ strongly from theoretical predictions based on the widely used Hertz-Knudsen formula (Knudsen 1909). The so-called sublimation coefficient of water ice describes the difference between measurements and theory and can be used as a correction coefficient, for example, to correctly model the temperature at the surface of a sublimating comet nucleus. Kossacki et al. (1999) proposed an empirical temperature dependence of the sublimation coefficient of pure water ice over the temperature range of 170–270 K, based on three different experimental datasets. The sublimation coefficient is close to 1 for temperatures lower than 195 K, decreases as the temperature increases from 195 K to 230 K, and then remains at a constant value of about 0.15 for higher temperatures. Gundlach et al. (2011) updated this empirical relation using the results of experiments conducted with mixtures of water ice and a dust component consisting of silica spheres. These results agree well

with those reported by Kossacki et al. (1999) for temperatures below 195 K and above 230 K, but show some discrepancies in between, in particular, with a faster decrease of the sublimation coefficient as temperature increases.

4. Discussion

As stated at the end of Sect. 2, the exposure of H_2O ice at the surface appears to be the most plausible hypothesis to explain the occurrence of the bright spots observed at the surface of 67P. Ices show the high reflectivity and neutral visible spectra required to explain the observations. At the heliocentric distances at which the observations were made, super-volatiles such as CO and CO_2 would sublimate very rapidly if exposed to direct solar illumination, ruling them out as candidates for the observed bright spots, which did not show any obvious change over a month. Water ice, in contrast, shows sublimation rates compatible with the OSIRIS observations at heliocentric distances larger than 3 AU. The sublimation rate of a planar surface of ice in vacuum can be calculated from the Hertz-Knudsen formula (Knudsen 1909) for temperatures up to 195 K (Gundlach et al. 2011). Through the vapor saturation pressure, the sublimation
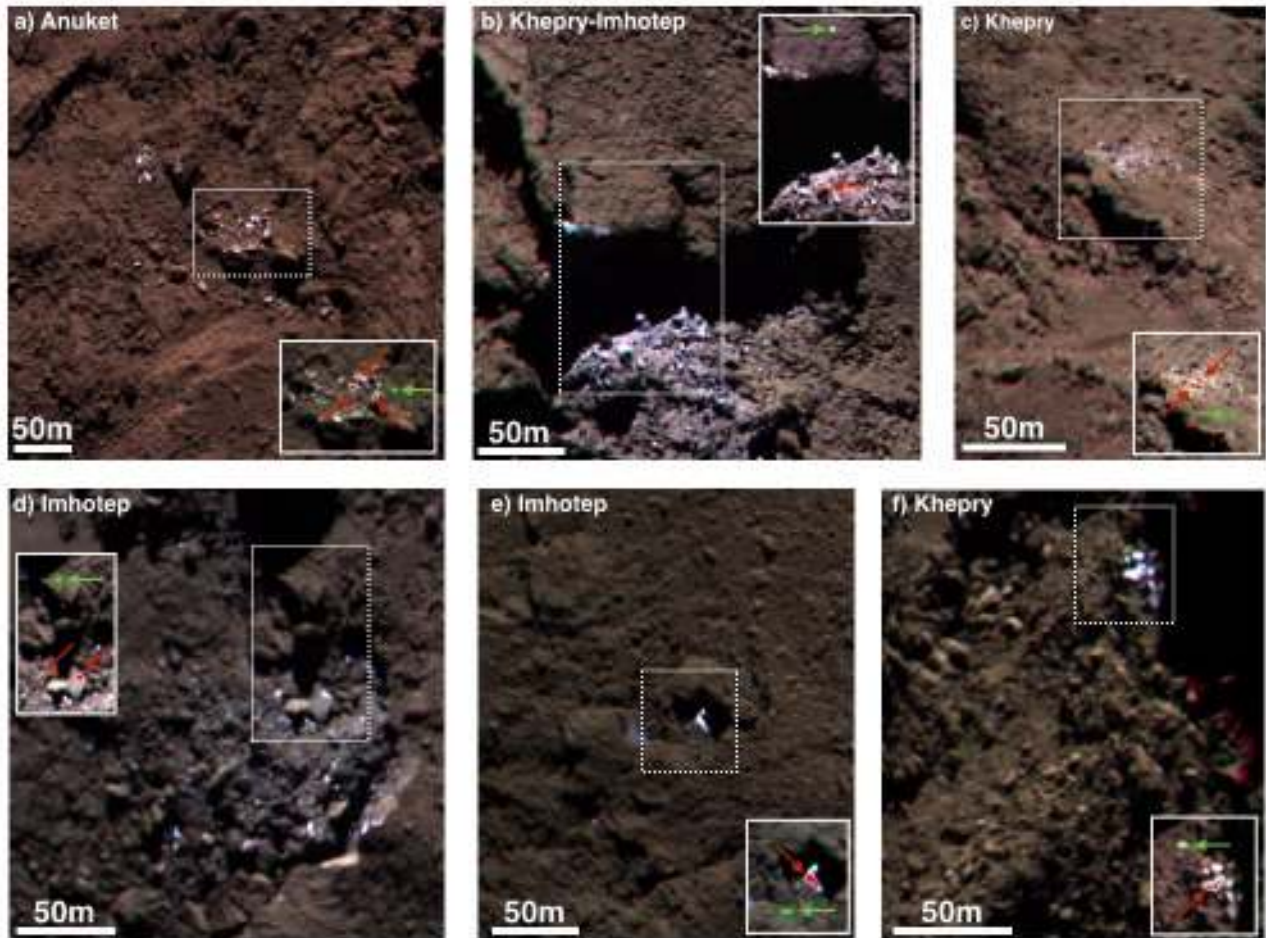
Fig. 8. RGB color-composites images of six different bright features produced using coregistered monochrome images acquired at 882.1 nm, 649.2 nm, and 360.0 nm as the R, G, and B color channels, respectively. Regions of interest (ROIs) of about 10 to 20 pixels defined over the bright features (red) and nearby over the surrounding dark terrain (green) are represented in the insets. They are used to calculate the average reflectance spectra and compute the spectral ratios shown in Fig. 9. **a)** Anuket. Subset of OSIRIS NAC image: NAC_2014-09-05T02.35.55.531Z_ID30_1397549700; **b)** Khepry-Imhotep. Subset of OSIRIS NAC image: NAC_2014-09-16T15.09.00.365Z_ID30_1397549700; **c)** Khepry. Subset of OSIRIS NAC image: NAC_2014-09-16T16.24.25.334Z_ID30_1397549500; **d)** Imhotep. Subset of OSIRIS NAC image: NAC_2014-09-05T06.35.55.557Z_ID30_1397549300; **e)** Imhotep. Subset of OSIRIS NAC image: NAC_2014-09-16T21.48.48.383Z_ID30_1397549100.

rate of the ice depends exponentially on temperature. For a surface of water ice with a porosity of 0.5, one obtains a sublimation rate of 0.07 mm/h at a temperature of 180 K, 0.4 mm/h at a temperature of 190 K and 0.9 mm/h at a temperature of 195 K. These values provide a good explanation to the observed distribution of bright features over the surface as the length of the day and the peak temperature reached during this day will determine where surface water ice can persist for periods of time of a few weeks. This agrees with the fact that most of the bright surface features observed are located in the areas that receive the lowest amounts of solar illumination. This is obvious in many images where the bright features are close to shadowed areas and in some cases are even completely surrounded by shadows. Exposures of H$_2$O ice might have occurred as well in areas receiving more abundant solar light, but may have already completely vanished because of fast sublimation at high peak temperature.

The results of laboratory experiments summarized in Sect. 3 offer additional support for this hypothesis by demonstrating how the sublimation of a mixture of H$_2$O ice with mineral and organic dust can to some extent reproduce the spectrophotometric properties observed at the surface of the nucleus. The structure

and physical properties that the samples acquire during the sublimation also provide us with interesting clues to understand the observations. The relatively homogeneous dark and red surface of the nucleus, only punctuated by the meter-scale bright dots, can be explained by the presence of a thin dust mantle composed of refractory mineral and organic matter. The bright spots correspond to areas from which the dust mantle was removed, exposing a subsurface material to the surface that is rich in H$_2$O ice. As shown by laboratory experiments, large chunks of the dust mantle are relatively easily removed because the mantle itself can show a strong internal cohesion but low cohesion with the icy material underneath.

In addition to the formation of a dust mantle by sublimation, as simulated in the laboratory, the dust mantle covering the surface of the nucleus also probably consists of dust re-deposited by a sort of airfall process in which particles emitted at velocity lower than the escape velocity fall back onto the nucleus (Thomas et al. 2015b; El-Maarry et al. 2015). The ability of such particles to build bounds between them once deposited at the surface and thus give a mechanical cohesion to the mantle is unknown and should be the topic of future experimental
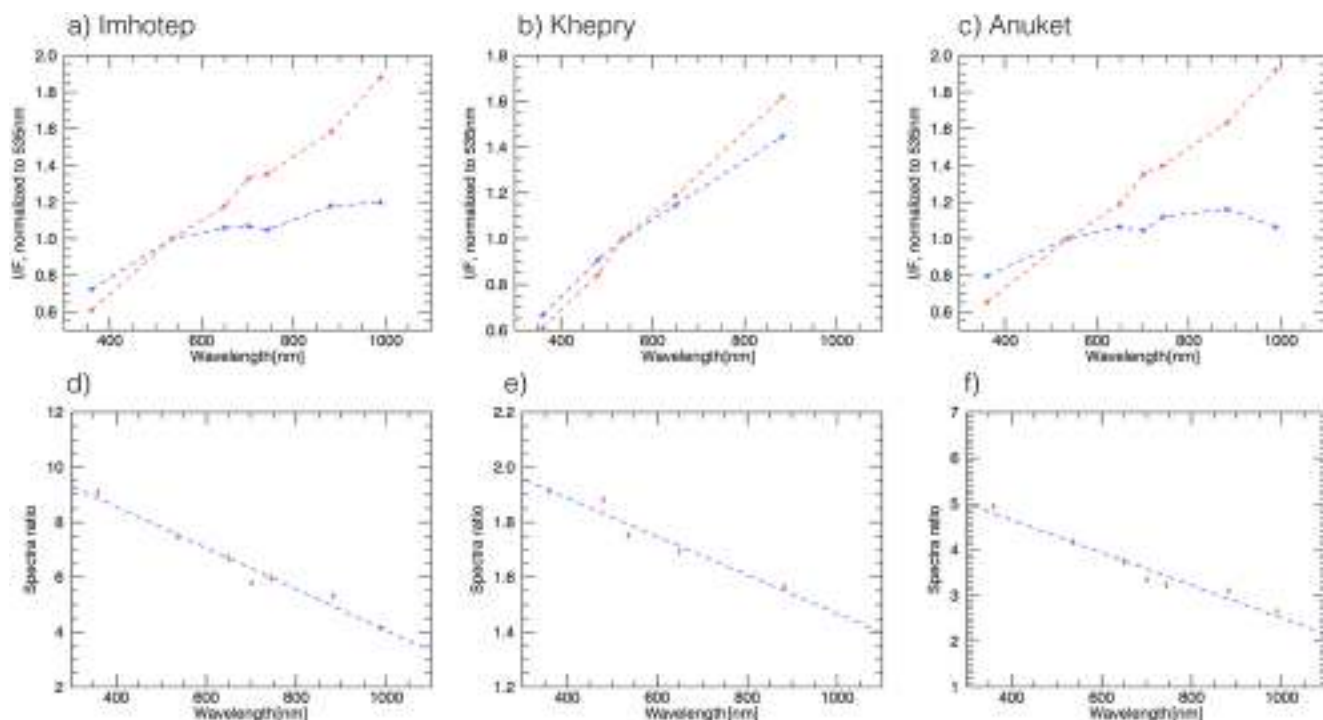
Fig. 9. a), b), and **c)** average normalized reflectance spectra of three different bright features (blue) and dark terrain nearby (red) for the examples shown in Figs. 7e, c, and a, respectively. Spectra of the bright features were averaged over a region of interest (ROI) of a few pixels defined inside the bright feature, avoiding its edges that are often affected by imperfect coregistration at the pixel scale. Spectra of the dark soil were averaged in a similar way over regions defined by avoiding all visible shadows in the image. All spectra were then normalized by their value of reflectance at 535.7 nm. **d), e)**, and **f)** corresponding ratios between the average spectra of the bright feature and the average spectra of the dark soil (crosses) and linear fit through these points (dashed lines).
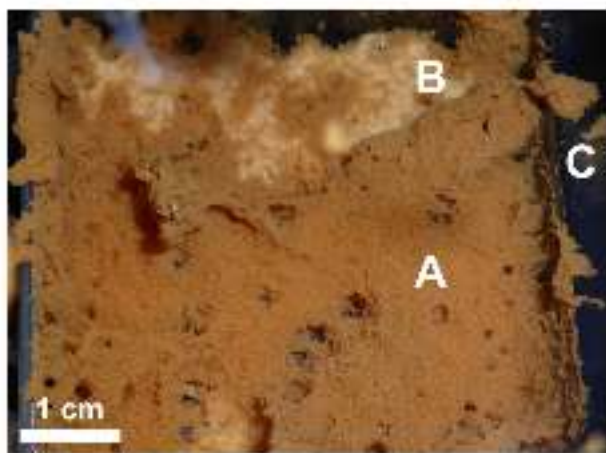

Fig. 10. Picture of a porous (>90%) mantle obtained after sublimation of an intra-mixture of 0.1% tholins and H_2O ice particles, 70 μm in diameter. The sublimation lasted about 40 h at pressure $<10^{-5}$ mbar and a surface temperature of 200–220 K in the SCITEAS simulation chamber. A: porous mantle made of water-free tholins; B: bright fresh ice particles exposed to the surface after ejection of a large fragment of the mantle; C: fragments of mantle ejected from the surface of the sample and deposited onto the sample holder.

Fig. 11. a) and **b)** normalized reflectance spectra corresponding to different steps of a sublimation experiment using μm-sized H_2O ice mixed with 5 wt.% basaltic airfall ash and 1 wt.% nanoparticle carbon as initial material. The red spectra in plots **a)** and **b)** are those of the final material at the end of the sublimation experiment. The blue spectrum in plot **a)** was acquired at the very beginning of the sublimation. The blue spectrum in plot **b)** was acquired about 10 h later. All spectra were normalized to their value of reflectance at 535.7 nm. **c)** and **d)** corresponding spectral ratios between the blue curves and red curves in plots **a)** and **b)**, respectively (crosses) and linear fit through these points (dashed lines).

investigations. Reaching a better match between the red slope observed at the surface of 67P and the one of laboratory analogs should also be an objective of future studies. The easiest way of reproducing the steep and linear slope observed in the visible spectral range in the laboratory seems to be by balancing the level of carbonization of the organic matter, as fully carbonized organic matter such as carbon black can reproduce the
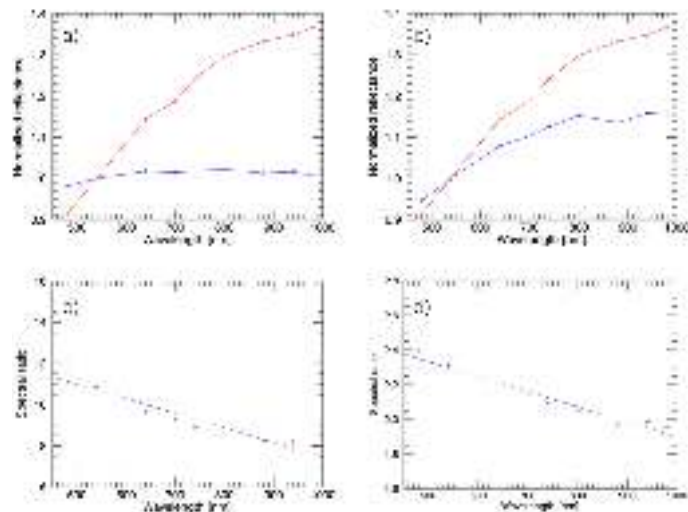
low albedo of the nucleus surface but does not reproduce the steep red slope that is displayed by more pristine organic matter such as the tholins that we have used in some experiments
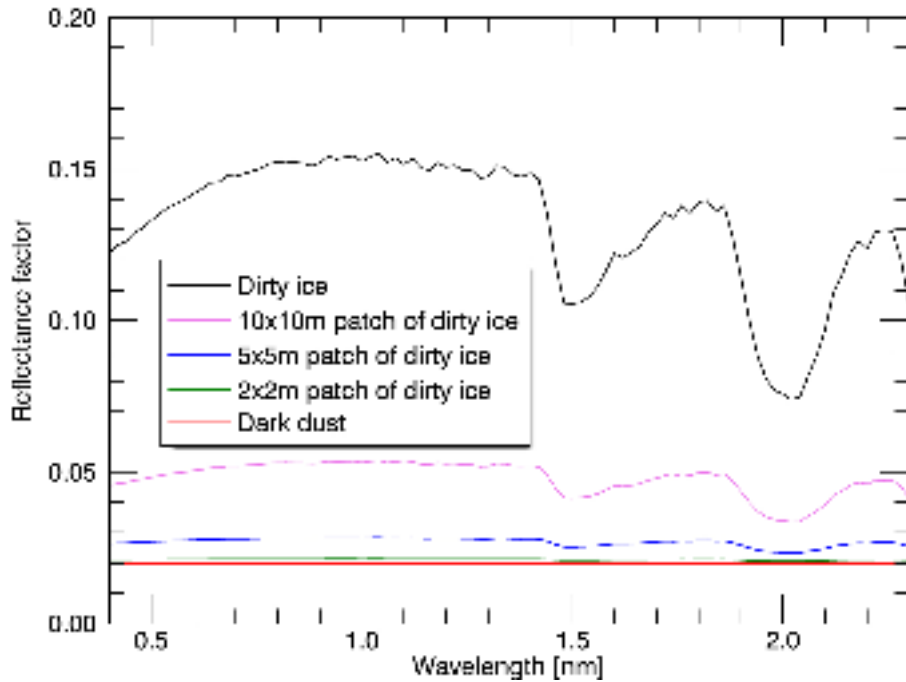
Fig. 12. Simulation of the effect of intra-pixel mixtures for bright features surrounded by dark terrain. The black curve is the reflectance spectrum of a dirty ice with a reflectance factor of 0.15 in the continuum, as measured in the laboratory during the same experiment as in Fig. 11. The intra-pixel mixture of a bright feature with surrounding dark terrain is simulated by a linear mixture of this spectrum with a neutral and dark spectrum (red curve). The resulting spectra are calculated and shown for three different areal fractions of a 20×20 m pixel: 1% (2×2 m), 6% (5×5 m) and 25% (10×10 m).

(Fig. 10). In addition, experiments should be systematically performed with variable amounts of dust mixed into the ice. Most of the experiments conducted so far investigated the case of minor amounts of dust mixed with large amounts of ice, which might not be the case of the nucleus of 67P. Although it is difficult to produce the organic analogs in large amounts, it is necessary to investigate the effect of the initial dust-to-ice ratio on the structure and mechanical properties of the dust mantle as well as the ejected grains.

Observations of the surface at the highest spatial resolution seem to indicate that most of the bright spots occupy fractions of the surface of meter-sized boulders, the rest of the boulder's surface showing surface reflectance and color similar to those of the surrounding terrain. The dust mantle would thus still cover most of the boulder's surface and would have been removed in a few areas, mostly around its periphery. It is tempting to propose a scenario that would explain both the origin of meter-sized boulders and the removal of large chunks of dust mantle from their surface. The clusters of boulders observed in many of the regions described as consisting of brittle material by Thomas et al. (2015b) or weakly consolidated material by El-Maarry et al. (2015) indicate a possible formation scenario. In these regions, a layering of the surface can often be observed with typical scales of a few meters to tens of meters. Differential erosion and mass wasting of the different strata is inferred (Thomas et al. 2015b). Often, mass wasting of a lower layer results in the formation of overhangs by the uppermost layer. Evidence of the collapse of these overhangs is seen at many places in the weakly consolidated regions (Groussin et al. 2015, Sect. 4.2). Debris fields are produced by the collapse, which are spread over tens of meters. Some of these debris fields contain bright boulders, albeit most of the boulders have a reflectance and color similar to the rest of the surface, as can be seen in Fig. 1.

The collapse and disruption of the overhangs produce fresh fractures in the brittle material, exposing ice-rich material from the interior. In addition, the dust mantle covering the material previously exposed at the surface might be removed as a result of the impacts during and following the collapse. Removal of this mantle is consistent with the high cohesion within the mantle but low cohesion between the mantle and the icy material underneath as seen in the laboratory (Fig. 10). The exposed water ice will eventually sublime with time, at different rates depending on the heliocentric distance, forming a new dust mantle at the surface of the icy blocks. We hypothesize that the bright spots that we see are these areas where the dust mantle has not reformed or has not yet reached a sufficient thickness to hide the icy material below. The best example we have of such an exposure of bright material by fracturing is Fig. 8b, where bright and blue material is seen both in the debris field below the overhang and on a vertical section of the uppermost brittle layer, at the place where this one cracked.

Additional support for this formation scenario comes from the analysis of the size-frequency distribution of the bright boulders shown in Fig. 2. Similar size-frequency distributions for four of the five fields studied indicate a common formation mechanism, and the value of the power-law index, 3.6 to 3.9, is similar to the value obtained by Pajola et al. (2015) in different locations such as the Nut mass wasting area, the Body2 B Khepry/Ash area, and the Hatmehit and Imhotep mass-wasting deposits identified close to similar decameter-high cliffs (see Table 5 in Pajola et al. 2015). Possible explanations for slopes steeper than -3.0 include thermal stress and activity fragmentation phenomena. The surface of a comet is an active and changing environment where outgassing volatiles and dust, rapidly mutating insolation and consequent thermal stress can lead from global cracks (Sierks et al. 2015; Thomas et al. 2015b) to very localized fractal fragmentation even on the boulders themselves when observed in high resolution (see Pajola et al. 2015, Fig. 1). This results in an increase of the population of smaller sized boulders with respect to the larger boulders, or likewise, a preferential disruption of the larger boulders, hence steepening the cumulative size-frequency distribution slopes and possibly leading to the values we observed in this analysis.

In contrast to the four other clusters investigated, the cluster in Imhotep shown in Fig. 8d shows a power-law index similar to those associated to terrestrial (Curran et al. 1977) or asteroidal impact-related phenomena (Klacka 1992) and that partially overlaps with the trend (Pajola et al. 2015, Fig. 10) measured in the

Hapi region of the comet. More generally, the Imhotep region is a very peculiar place in terms of occurrences of bright features (Auger et al. 2015, Sect. 3.4). This is interesting considering that this region shows many other particularities such as smooth terrains with circular features that are not observed anywhere else on the nucleus (Auger et al. 2015, Sects. 3.1 and 3.6). The relation between the abundance of bright features in this region and the other peculiar morphologies is still unclear but supports the idea that Imhotep experiences ongoing mass wasting and is likely representative of other regions in the southern hemisphere, which would be active around perihelion.

The formation of hard crusts of ice under the uppermost dust mantles in laboratory experiments may offer a plausible hypothesis for the brittle mechanical behavior of the surface in regions that have obviously already experienced extensive sublimation during previous passages of the comet at perihelion. Beyond effects on the thermal and mechanical properties of the surface material, sintering or recondensation processes are certainly also able to change its reflectivity by segregating the ice from the dust. It is well possible that the brighter and bluer material seen at the surface of the boulders is not the primordial material that forms the bulk of the nucleus, but a highly reprocessed surface material, resulting from strong metamorphism produced by intense solar heating. Indeed, all laboratory measurements made on mixtures of H_2O ice and dark organic materials show that only a few weight percent of dust are sufficient to reduce the albedo of the ice below 10% when ice and dust are intimately mixed. As many higher fractions of dust are expected in the material from which comets are formed and because the dark dust particles might be embedded in the grains of ice (Greenberg 1982), one would indeed expect the bulk material of the nucleus to be much darker than the brightest features observed, which have reflectance factors of around 13%.

We note, however, that the formation of a thick hard crust requires specific conditions of temperature in the subsurface to occur and, as indicated by recent laboratory experiments (Poch et al. 2015), seems to be strongly influenced by the mixing mode between the ice and the dust. It is thus currently unclear if and where sintering of the water ice in the subsurface might have occurred on the comet in thicknesses large enough to explain the observations reported here. Given the potential importance of this process for various properties of the material, this question deserves high attention and additional studies through laboratory experiments, modeling, and analysis of Rosetta remote-sensing and in situ Philae data.

Some of the isolated spots, boulders with bright patches at their surface or small clusters of only a few bright spots, however, completely lack a geomorphological context that could explain their formation. The best example here is Fig. 3b where a bright spot is observed over the smooth terrain in the Ash region. For these cases, we hypothesize that icy blocks were produced at a distant place on the nucleus, ejected with a velocity sufficient to fly over large distances, but insufficient to escape its gravity field. The blocks may have bounced a few times before resting at their final location and could have fragmented into smaller blocks on landing. For example, the features shown in Figs. 8a and c could have originated from this process. Evidence for the emission of small particles at low velocity and redeposition by a sort of airfall have been obtained at many places around the nucleus (Thomas et al. 2015b,a). The large smooth areas of the Ash region and similar-looking regions have been hypothesized to result from this process. Mass loss of large chunks of surface material has also been proposed to account for the morphology of large depressions on the nucleus. All these observations

are consistent and, taken together, emphasize the importance of transport of material at the surface of the nucleus.

We can consider two possibilities for the timing of the bright boulders formation: during the passage at perihelion or at larger heliocentric distance since the last passage. The first possibility involves activity due to water ice sublimation and requires the emission and transport of the icy block into regions of the nucleus that remain permanently shadowed around and after the closest approach of the nucleus to the Sun until it reached a large heliocentric distance at which water is stable at the surface. Therefore, this possibility only involves a minor fraction of the nucleus surface. The second possibility implies the role of super-volatiles such as CO_2 and CO in the activity at large heliocentric distances from the Sun. In this case, bright boulders can be produced and deposited at any position on the nucleus as the surface temperature is still too low for water ice sublimation to occur. As the nucleus progresses toward the Sun, however, most of the bright features will disappear as the sublimation rate rapidly increases and only those that are located in permanently shadowed areas can survive the passage at perihelion.

It is already clear that many of the observed bright features are not located at places that will be shadowed at perihelion, in particular the large ones in the Imhotep region. Future observations of these bright features as the comet is progressing toward the Sun should thus show them vanishing. As new regions emerge from the polar night, new bright features might also be observable and may be produced. In the case of bright icy blocks produced at shorter heliocentric distance, the evolution should be much faster than what is observed here. All these future observations are ways of testing if the hypotheses formulated here are correct.

In addition to OSIRIS observations, other instruments might also be able to provide information on the bright features described here, in particular, near-infrared observations by the VIRTIS instrument. The calculations made in Sect. 3 using laboratory characterizations (Fig. 12) show, however, that the meter-scaled bright features might be right at the limit of what is detectable by VIRTIS. Indeed, the near-infrared part of VIRTIS reflectance spectra contains the unique spectral signatures of various ices that can be used to unambiguously identify them. However, the spatial resolution of this instrument is much lower than that of the OSIRIS NAC camera. Hyperspectral cubes acquired from August to September 2014 had a surface spatial resolution varying between 15 and 30 m per pixel (Capaccioni et al. 2015). As a result, the bright features studied in this article would only occupy a fraction of a VIRTIS pixel. Analyzing in which conditions the putative water ice exposures observed by OSIRIS NAC could be confirmed by VIRTIS is thus crucial to conclude about the agreement between these datasets. The case of a subpixel geographic binary mixture is the simplest case to treat in radiative transfer. The reflectance spectrum of the pixel is the linear combination of the reflectance spectra of the two end-members, weighted by the fraction of the surface of the pixel they occupy. For the icy end-member, we used an experimental reflectance spectrum displaying the same reflectance factor in the continuum around $0.8\,\mu m$ as observed over bright features at the surface of 67P. For the non-icy end-member, we simply used a constant reflectance factor of 0.02 as a first-order approximation. The results of these simple calculations are shown in Fig. 12 for different sizes of the bright features and a VIRTIS pixel of 20×20 m. The spectral signatures of a 2×2 m spot of dirty water ice isolated inside a 20×20 m pixel are very strongly attenuated and will be hard to detect, even considering a low instrumental noise level. A 5×5 m exposure of the

same dirty ice, however, would display distinctive absorption at 1.5 and 2 μm that could be detectable if the level of noise is lower than about 1% in units of reflectance factor. VIRTIS observations acquired at short distance from the nucleus should achieve higher spatial resolutions than the 20 × 20 m/pixel images presented by Capaccioni et al. (2015) , however, and should be able to detect water ice in a number of the bright features described here if our hypothesis is correct. In addition to the 1.5 and 2 μm bands of H$_2$O ice, VIRTIS is also able to acquire measurements in the 3 μm region where fundamental absorptions by the H$_2$O molecule give rise to much stronger absorption. The analysis of this region of the spectrum is complicated by numerous organics absorptions (Capaccioni et al. 2015). This range of wavelengths is not covered by the laboratory measurements reported here, and complementary measurements with different instrumentation will be required to quantitatively analyze the detectability of H$_2$O ice in this range.

5. Conclusion

Our preferred interpretation of the numerous meter-sized bright spots identified in OSIRIS NAC images acquired between August and November 2014 is the exposure of water ice at the surface. This interpretation is compatible with the following properties of the bright features:

- A reflectance of up to ten times the reflectance of the surrounding terrain.
- A significantly bluer spectrum than in the surrounding red terrain.
- An apparent stability of their morphology and photometric properties over a few weeks.
- A strong preferential location in areas receiving low insolation.

We suggest that meter-scale exposure of water ice at the surface of boulders is the result of the absence of the dark mantle of refractory dust that covers the entire surface of the nucleus and hides the icy material beneath it. Surface activity in the form of a fragmentation of the upper layers of the nucleus to form collapsed walls and mass wasting seems to be responsible for these exposures of ice. After their formation, the boulders produced either remained in place or flew and bounced to distant locations. The activity could be recent, triggered by super-volatiles such as CO$_2$ and CO at large heliocentric distance, or they might be more ancient, at the time of the last passage of the comet at perihelion and triggered by water sublimation. In the latter case, only the exposures of ice located in areas permanently shadowed at perihelion could have been preserved. The interpretations of OSIRIS observations made here are supported by laboratory experiments that show how mixtures of water ice and dust exposed to vacuum at low temperature acquire a vertical stratification. After some hours of irradiation, an uppermost dark mantle of refractory dust completely covers an ice-rich subsurface in which recondensation and sintering might have occurred, strongly affecting the mechanical, thermal, and photometric properties of the material. The conditions for the sintering to take place as well as the influence of the sample initial composition on the structure and properties of the dust mantle will need to be investigated in detail in the future. As the comet approaches perihelion, the increase in insolation in the illuminated regions should induce a fast sublimation of the water-ice exposures. Monitoring the evolution of the bright spots over time will thus be the best

way to assess whether the hypotheses formulated in this article are correct.

References

Auger, A.-T., Groussin, O., Jorda, L., et al. 2015, A&A, 583, A35
Barucci, M. A., Dotto, E., & Levasseur-Regourd, A. C. 2011, A&ARv, 19, 48
Beckmann, W., & Lacmann, R. 1982, J. Crystal Growth, 58, 433
Brown, R. H., Lauretta, D. S., Schmidt, B., & Moores, J. 2012, Planet. Space Sci., 60, 166
Capaccioni, F., Coradini, A., Filacchione, G., et al. 2015, Science, 347, 628
Carrasco, N., Schmitz-Afonso, I., Bonnet, J.-Y., et al. 2009, J. Phys. Chem. A, 113, 11195
Coradini, A., Capaccioni, F., Drossart, P., et al. 1999, Adv. Space Res., 24, 1095
Curran, D. R., Seaman, L., & Shockey, D. A. 1977, Phys. Today, 30, 46
Davidsson, B. J. R., Gutiérrez, J., Sierks, H., et al. 2015, A&A, 583, A16
El-Maarry, M., Thomas, N., Giacomini, L., et al. 2015, A&A, 583, A26
Fornasier, S., Hasselmann, P. H., Barucci, M. A., et al. 2015, A&A, 583, A30
Greenberg, J. M. 1982, in IAU Colloq. 61: Comet Discoveries, Statistics, and Observational Selection, ed. L. L. Wilkening, 131
Groussin, O., Jorda, L., Auger, A.-T., et al. 2015, A&A, 583, A32
Gruen, E., Bar-Nun, A., Benkhoff, J., et al. 1991, in IAU Colloq. 116, Comets in the post-Halley era, eds. R. L. Newburn, Jr., M. Neugebauer, & J. Rahe, Astrophys. Space Sci. Lib., 167, 277
Gundlach, B., Skorov, Y. V., & Blum, J. 2011, Icarus, 213, 710
Keller, H. U., & Markiewicz, W. J. 1991, Geophys. Res. Lett., 18, 249
Keller, H. U., Barbieri, C., Lamy, P., et al. 2007, Space Sci. Rev., 128, 433
Klacka, J. 1992, Earth Moon Planets, 56, 47
Knudsen, M. 1909, Ann. Phys., 333, 999
Kömle, N. I., Kargl, G., Thiel, K., & Seiferlin, K. 1996, Planet. Space Sci., 44, 675
Kossacki, K. J., & Leliwa-Kopystynski, J. 2014, Icarus, 233, 101
Kossacki, K. J., Kömle, N. I., Leliwa-Kopystyński, J., & Kargl, G. 1997, Icarus, 128, 127
Kossacki, K. J., Markiewicz, W. J., Skorov, Y., & Kömle, N. I. 1999, Planet. Space Sci., 47, 1521
Lamy, P. L., Toth, I., Fernandez, Y. R., & Weaver, H. A. 2004, The sizes, shapes, albedos, and colors of cometary nuclei, ed. G. W. Kronk, 223
Li, J.-Y., A'Hearn, M. F., Belton, M. J. S., et al. 2007, Icarus, 187, 41
Li, J.-Y., Besse, S., A'Hearn, M. F., et al. 2013, Icarus, 222, 559
Moores, J. E., Brown, R. H., Lauretta, D. S., & Smith, P. H. 2012, Planet. Sci., 1, 2
Pajola, M., Vincent, J.-B., Güttler, C., et al. 2015, A&A, 583, A37
Poch, O., Pommerol, A., Jost, B., et al. 2015, Icarus, submitted
Pommerol, A., Thomas, N., Affolter, M., et al. 2011, Planet. Space Sci., 59, 1601
Pommerol, A., Jost, B., Poch, O., et al. 2015, Planet. Space Sci., in press
Seiferlin, K., Spohn, T., & Benkhoff, J. 1995, Adv. Space Res., 15, 35
Sierks, H., Barbieri, C., Lamy, P. L., et al. 2015, Science, 347, 1044
Sunshine, J. M., A'Hearn, M. F., Groussin, O., et al. 2006, Science, 311, 1453
Sunshine, J. M., Feaga, L. M., Groussin, O., et al. 2012, LPI Contributions, 1667, 6438
Thomas, N., Davidsson, B., El-Maarry, M., et al. 2015a, A&A, 583, A17
Thomas, N., Sierks, H., Barbieri, C., et al. 2015b, Science, 347, 440
Tubiana, C., Güttler, C., Kovacs, G., et al. 2015, A&A, 583, A46

1   Physikalisches Institut, University of Bern, Sidlerstrasse 5, 3012 Bern, Switzerland
    e-mail: `antoine.pommerol@space.unibe.ch`
2   Centro di Ateneo di Studi ed Attivitá Spaziali, Giuseppe Colombo (CISAS), University of Padova, 35131 Padova, Italy

[3] Aix-Marseille Université, CNRS, LAM, UMR 7326, 38 rue Frédéric Joliot-Curie, 13388 Marseille, France

[4] Max-Planck-Institut für Sonnensystemforschung, Justus-von-Liebig-Weg, 3, 37077 Göttingen, Germany

[5] LESIA, Obs. de Paris, CNRS, Univ. Paris 06, Univ. Paris-Diderot, 5 place J. Janssen, 92195 Meudon, France

[6] Department of Physics and Astronomy, Uppsala University, 75120 Uppsala, Sweden

[7] LATMOS, CNRS/UVSQ/IPSL, 11 boulevard d'Alembert, 78280 Guyancourt, France

[8] Department of Physics and Astronomy, University of Padova, Vicolo dell'Osservatorio 3, 35122 Padova, Italy

[9] Deutsches Zentrum für Luft- und Raumfahrt (DLR), Institut für Planetenforschung, Rutherfordstraße 2, 12489 Berlin, Germany

[10] Institut für Geophysik und extraterrestrische Physik (IGEP), Technische Universität Braunschweig, Mendelssohnstr. 3, 38106 Braunschweig, Germany

[11] The University of Kent, School of Physical Sciences, Canterbury, Kent, CT2 7NZ, UK

[12] Department of Information Engineering, University of Padova, via Gradenigo 6/B, 35131 Padova, Italy

[13] CNR-IFN UOS Padova LUXOR, via Trasea, 7, 35131 Padova , Italy

[14] International Space Science Institute, Hallerstraße 6, 3012 Bern, Switzerland

[15] Centro de Astrobiología, CSIC-INTA, 28850 Torrejón de Ardoz, Madrid, Spain

[16] Scientific Support Office, European Space Agency, 2201 Noordwijk, The Netherlands

[17] PAS Space Research Center, Bartycka 18A, 00716 Warszawa, Poland

[18] Department of Astronomy, University of Maryland, College Park, MD 20742-2421, USA

[19] INAF–Osservatorio Astronomico, vicolo dell'Osservatorio 5, 35122 Padova, Italy

[20] University of Trento, via Mesiano, 77, 38100 Trento, Italy

[21] Department of Industrial Engineering – University of Padova, via Venezia 1, 35131 Padova, Italy

[22] INAF–Osservatorio Astronomico, via Tiepolo 11, 34014 Trieste, Italy

[23] Instituto de Astrofísica de Andalucía (CSIC), c/ Glorieta de la Astronomía s/n, 18008 Granada, Spain

[24] National Central University, Graduate Institute of Astronomy, 300 Chung-Da Rd, 32054 Chung-Li, Taiwan

[25] Operations Department, European Space Astronomy Centre/ESA, 28691 Villanueva de la Canada, Madrid, Spain

[26] Institut für Datentechnik und Kommunikationsnetze der TU Braunschweig, Hans-Sommer-Str. 66, 38106 Braunschweig, Germany